Spatial Light Modulator Based Propagation of Partially Coherent Speckle Fields in a 4f Setup

Paul Schulze

Universität Bremen

bias
Bremer Institut für
angewandte Strahltechnik

Spatial Light Modulator Based Propagation of Partially Coherent Speckle Fields in a 4f setup

Paul Schulze

1. Reviewer   **Prof. Dr. rer. nat. habil.
Ralf B. Bergmann**
BIAS – Bremer Institut für
angewandte Strahltechnik

2. Reviewer   **Prof. Dr.-Ing. habil.
Andreas Fischer**
BIMAQ – Bremer Institut für Messtechnik,
Automatisierung und Qualitätswissenschaft

Supervisor   Dr. rer. nat. Thorsten Klein

Urheberrechtliche Erklärung

Erklärung gem. § 10 (10) Allgemeiner Teil der BPO vom 27.10.2010

Hiermit versichere ich, dass ich meine Bachelorarbeit ohne fremde Hilfe angefertigt habe, und dass ich keine anderen als die von mir angegebenen Quellen und Hilfsmittel benutzt habe.

Alle Stellen, die wörtlich oder sinngemäß aus Veröffentlichungen entnommen sind, habe ich unter Angabe der Quellen als solche kenntlich gemacht.

Die Bachelorarbeit darf nach Abgabe nicht mehr verändert werden.

Paul Schulze, Matrikelnummer 4273910

_____   _____
Datum, Ort   Unterschrift

Erklärung zur Veröffentlichung von Abschlussarbeiten

Ich bin damit einverstanden, dass meine Abschlussarbeit im Universitätsarchiv für wissenschaftliche Zwecke von Dritten eingesehen werden darf.

Paul Schulze, Matrikelnummer 4273910

_____   _____
Datum, Ort   Unterschrift

Acknowledgement

Abstract

Contrast measurements of interference patterns emerging from the surface can be used to evaluate the three dimensional shape of an object. Traditionally, moving the focal plane through the object involves a mechanical movement in the imaging system. In my thesis, I show that a spatial light modulator (SLM) utilizing the transfer function of propagation can move the focal plane with no reduction in image quality and without the need for any mechanical movement. The SLM is integrated in the Fourier plane of a 4f imaging system. The speckle patterns (interference patterns) play a central role in the evaluation process of the three dimensional measurement. I report my findings from a simulation, which relate the size of the speckle to the wavelength of light used as illumination, the size of the Fourier aperture and the focal length of the utilized lenses in the 4f setup. A method for speckle size detection is presented. For partially coherent light, a predictable area of high contrast forms around the objects' surface, with the rest of the wave field being of lower contrast. The simulated results are supported by experimental evidence. I experimentally demonstrate a visible difference in contrast and image sharpness for microscopic surface features of different height. This paves the road for the development of a fully functional measuring method that is precise, fast, robust against vibrations and exhibits an extended depth of focus.

Contents

1 Introduction

1.1 Background

Quality assurance is a high priority in parts manufacturing. Measuring the three-dimensional shape of a part is often sufficient to judge its ability to function as intended. Micro parts - components that are smaller than one millimeter in all three dimensions - are among the most expensive to replace because they become elements of larger assemblies later during the production process. Figure 1.1 shows thin metal cups as example for micro cups.
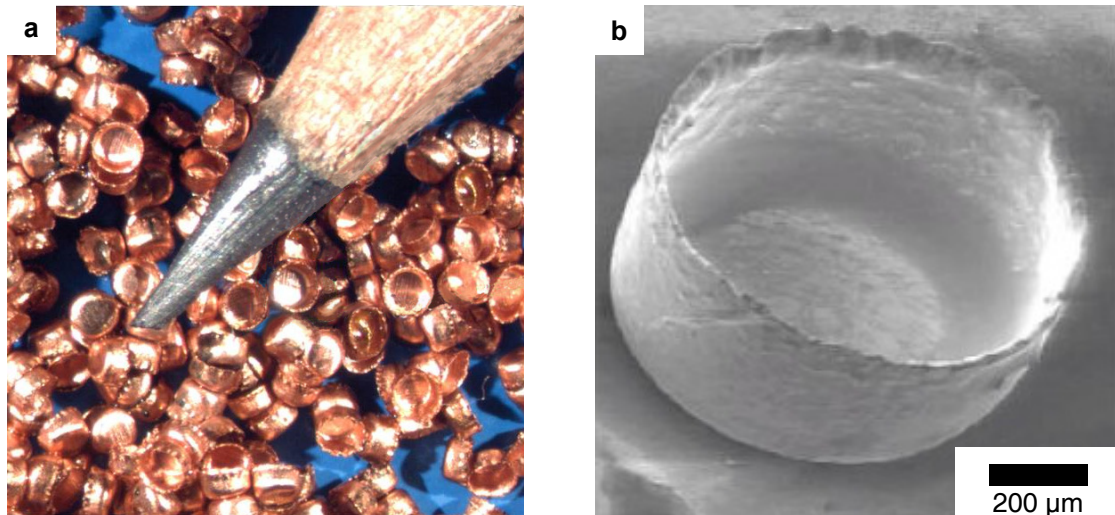

Figure 1.1: Example of micro forming parts. a, Thin metal micro-cups with a size of less than 1 mm in all three dimensions. **b**, scanning electron microscope image of the part.

The evaluation of functionality for these parts is therefore of particular importance. The requirements for such a task, however, are especially high. A measuring method that exhibits
  i)   a high measurement accuracy
  ii)   a high measurement speed
  iii) robustness against vibrations and
  iv)   an extended depth of focus

is needed. No method currently in use can fulfill all of the requirements at the same time. Tactile methods and confocal microscopy are too slow for the fast paced production lines of industrial manufacturing centers. Interferometric methods - of which three distinct categories have been established - are generally better suited for these demands:

1) Evaluation of the phase distribution of monochromatic light
Methods of the first category are based on the evaluation of the phase distribution of monochromatic light in the object plane. This includes digital holography [1] and phase shifting interferometry [2, 3]. The wave field reflected by the object interferes with a known reference wave. The phase information is then encoded into the interference pattern in the image plane. The phase can be calculated from this interference pattern using a variety of techniques [4, 5, 6]. The phase information can be processed further to gain insight into the optical path difference, which ultimately leads to a model of the three dimensional shape of the object. For this method, the illuminating light source is required to be of high temporal and spatial coherence. A monochromatic laser is therefore often necessary. However, reliably measuring small parts can present a

challenge to this method. An additional problem is the dependence on the interference of two different optical paths, which is sensitive to vibrations and thermal fluctuations.

2) Scanning White Light Interferometry and Optical Coherence Tomography

The second category includes methods that extract the optical path difference from the coherence function on partially coherent light, e.g. scanning white light interferometry (SWLI) [7, 8, 9, 10] and time domain (TD) and spectral (or Fourier) domain (SD) optical coherence tomography (OCT) [11, 12, 13, 14]. These methods are based on a Michelson interferometer, where one mirror is replaced by the object. A long spatial coherence length and a short temporal coherence length are required for the illumination. Interference will only be observed in areas with an optical path difference of half the temporal coherence length to the reference beam. Moving the mirror along its optical axis results in an altered interference pattern in the imaging plane. The set of interference patterns obtained after movement to multiple locations can be used to calculate a three dimensional representation of the objects' shape. One of the disadvantages of this method is the need for a large number of measurements in combination with the mechanical movement of the mirror, which is both slow and inaccurate. SWLI and OCT are therefore both not suited for production in-line use [15]. Following the same argument made for the first category, SWLI and OCT are also prone to vibrations and thermal fluctuations.

3) Spatial Coherence Profilometry

The third category of methods is based on a concept called spatial coherence profilometry (SCP) [16, 17, 18]. In contrast to the methods of category two, light with a short spatial coherence length is used for illumination. The test object replaces one mirror in the Michelson interferometer, but no mechanical movement of the mirror nor the object is required for a complete measurement. Several Fresnel zone plates and a rotating ground glass vary the spatial coherence and the resulting variations in the interference patterns are utilized for shape retrieval. The lack of mechanical movement opens up the possibility for high speed measurements. Yet, the interferometric approach adopted by this technique has the disadvantage that it requires high mechanical stability. In addition, the focal depth is short, preventing this method from being utilized as an industrial quality inspection method.

The characteristics of each of the above described categories are summarized in Table 1.1.

Table 1.1: Properties of phase evaluation, scanning white light interferometry (SWLI), optical coherence tomography (OCT) and spatial coherence profilometry (SCP).

	Phase Evaluation	SWLI and OCT	SCP
Accuracy	✗	✓	✓
High speed	✓	✗	✓
Robustness	✗[a]	✗	✗
Extended depth of focus	✓	✓	✗

[a] Technique becomes vibration insensitive in case of using pulsed laser for illumination.

In-line quality control in fast production lines requires fast and precise methods that exhibit robustness against vibrations and an extended depth of focus. None of the currently existing methods can fulfill all of the requirements at the same time.

In Ref. [19], a novel approach to this problem is presented. A common path configuration is used to embed the optical path difference in the spatial coherence function. The light is manipulated by an SLM in the Fourier plane of a 4f setup. The SLM can perform depth scans without the need for any mechanical movement in the system. The common path configuration does not

require a high mechanical stability and is therefore much less prone to vibrations and thermal fluctuations. Another advantage is the low demand in terms of spatial and temporal coherence of the light source. It is therefore possible to use eye-safe, low-cost light sources such as Light Emitting Diodes (LEDs) for illumination. Switching the SLM with a digital micromirror device (DMD) improves the speed of the measurement further. The DMD can achieve refresh rates in the range of 1 kHz, which can be exploited to reach exceptional measuring speeds.

1.2 Scope of the Thesis

The aim of the work presented here is the development of an experimental setup that can perform depth scans by recording intensity distributions in several focal planes. The emerging intensity patterns in the imaging plane are analyzed in view of the development of a measuring method utilizing a light source with a short spatial coherence length. The following hypotheses will be investigated:

Hypothesis 1: The Speckle size can be predicted from wavelength of light, aperture size and focal length in the 4f setup.

Hypothesis 2: Partially coherent illumination leads to a predictable area of high contrast interference around the objects surface.

Hypothesis 3: The focal plane can be moved in the 4f setup by a spatial light modulator utilizing the transfer function of propagation.

The validation of these hypotheses will lay the groundwork for further developed setups that include high speed components and for the eventual evaluation part of the measuring method.

1.3 Outline

In this thesis, I start with an overview of the theoretical basis in Chapter 2. SLM-based propagation of partially coherent light and Fourier optics in general are reviewed. I transition from a continuous description to a discrete model in Chapter 3.1. This allows a numerical simulation to be carried out. I explain the experimental setup in Chapter 3.2. I also explain the algorithm to detect simulated speckle sizes. The predictions made by the model and the simulated results are presented in Chapter 4.1. I calculate coherent and partially coherent wave fields and examine various aspects of the emerging speckle patterns. This is repeated in part in the experiment. Chapter 4.2 presents the experimental results. A thorough discussion is considered in Chapter 5. Finally, I place the results in a broader context and indicate areas where further research is needed in Chapter 6.

2 Theory of light propagation

This chapter aims to provide a brief overview of the theoretical basis of this work. I present the mechanism behind SLM propagation and the concept of spatial coherence in the context of the 4f setup.

The Impulse Response

The concept of SLM based propagation of light is based on Fourier optics. Assume g_1 to be the input function and g_2 to be the output function of an invariant linear system. The two functions are thus related by

$$g_2(x) = S\{g_1(x)\}. \tag{2.1}$$

Using the properties of the delta distribution to represent g_1, we obtain

$$g_2(x) = S\left\{\int_{-\infty}^{\infty} g_1(x')\delta(x' - x)dx'\right\}. \tag{2.2}$$

Since S is a linear operation, it can be brought into the integral in such a way that

$$g_2(x) = \int_{-\infty}^{\infty} g_1(x')h(x' - x)dx', \tag{2.3}$$

where $h(x' - x) = S\{\delta(x' - x)\}$ is called the *impulse response* of the system. We have now brought Equation 2.1 into the simple relation

$$g_2 = g_1 \circledast h, \tag{2.4}$$

where $\circledast$ denotes the convolution operator. The output function g_2 can easily be computed using the convolution theorem

$$G_2 = G_1 \cdot H. \tag{2.5}$$

Where G_1, G_2 and H are the Fourier transformed functions of g_1, g_2 and h, respectively. H is called the *transfer function* of a system.

Because of the linearity of the system, all of the steps described above can be extended into two dimensions. For a more extensive and rigorous description, the reader is regarded to [20].

The Transfer Function of Propagation

In optical systems, the propagation of light from one plane $\{\boldsymbol{x}_a\}$ to another plane $\{\boldsymbol{x}_b\}$ can be described by the impulse response of propagation

$$h_z = \frac{z}{i\lambda} \frac{\exp(ik|\boldsymbol{r}|)}{|\boldsymbol{r}|^2}, \tag{2.6}$$

where $|\boldsymbol{r}|$ is defined as $|\boldsymbol{x}_a - \boldsymbol{x}_b|$, z is the distance between the two planes, λ is the wavelength of light, and k is the wave number. This is illustrated in Figure 2.1. The corresponding transfer function

$$H_z = \exp\left[ikz\sqrt{1 - \lambda^2|\boldsymbol{\xi}|^2}\right] \tag{2.7}$$

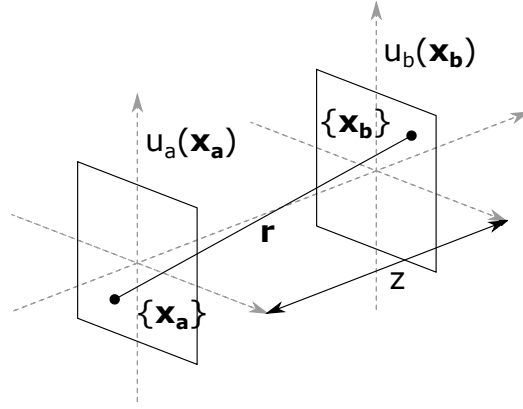is the Fourier transform of the impulse response [21].

Figure 2.1: Plane to plane propagation between two parallel planes. The planes are separated by a distance of z. u_a and u_b refer to the respective complex amplitude distributions in $\{x_a\}$ and $\{x_b\}$. r connects a location in the $\{x_a\}$ domain with a location in $\{x_b\}$.

The wave field in u_b can thus be represented by

$$u_b = \mathcal{F}^{-1}\{U_b\} = \mathcal{F}^{-1}\{U_a \cdot H_z\}, \tag{2.8}$$

taking advantage of Equation 2.5. A propagated representation u_b of the wave field can thus be calculated by a simple multiplication of the Fourier transformed wave field U_a with the transfer function H_z.

Experimental Implementation Using a Spatial Light Modulator

The operation (2.8) is a pure phase modulation of U_a and can be practically performed by a reflective phase-only liquid crystal SLM in the mutual Fourier plane of a 4f setup, as indicated in Figure 2.2. This mechanism has first been proposed at BIAS for phase retrieval applications [22, 23]. The 4f setup takes advantage of the Fourier transforming properties of lenses, creating a Fourier transformed representation

$$\hat{u}_a(\mathbf{v}) = \frac{A}{i\lambda f}\mathcal{F}\{u_a(\mathbf{x_a})\}\left(\frac{\mathbf{v}}{\lambda f}\right) \tag{2.9}$$

of the wave field u_a across its back focal plane [20] where A denotes the Amplitude in the front focal plane. The wave field is broken down into its spatial frequency components, which can be manipulated by the aperture and the SLM. The second lens performs another Fourier transform and projects the result onto the camera CCD.
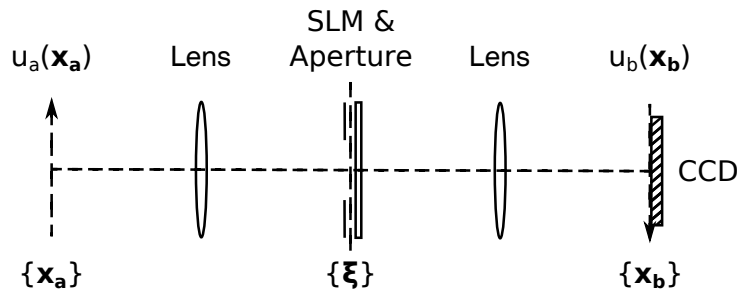

Figure 2.2: Working principle of a 4f setup. A Fourier representation of the wave field u_a is generated in the back focal plane of the first lens, where it can be manipulated with an aperture and an SLM. The manipulated wave field is then transformed back by the second lens and projected onto a charged coupled device (CCD) sensor of a recording camera.

Spatial Coherence and Contrast in the Imaging Plane

Spatial coherence is a measure for the mutual correlation of spatially separated parts of the same wave field. The spatial coherence length is defined as the distance, where two separated parts of the wave field can generate an interference pattern. The intensity I of such an interference pattern can be calculated according to the expression

$$I = I_1 + I_2 + 2\sqrt{I_1 I_2}|\gamma| \cos \Delta\phi, \tag{2.10}$$

where I_1 and I_2 refer to the intensities of the added wave fields, $\Delta\phi$ refers to their phase difference, and $|\gamma|$ is a measure for the mutual coherence of the added wave fields. The gamma value can be approximated in the input plane of the 4f setup by

$$|\gamma| = \left| \frac{2J_0(\pi dS/(\lambda R)}{\pi dS/(\lambda R)} \right|, \tag{2.11}$$

where J_0 is the 0th order Bessel function, and S and R refer to the distance and width of the light source, respectively [24]. The parameter d describes the distance between the added parts of the wave field. This function reaches the minimum of the first order at $d_1 = 0.61\frac{\lambda R}{S}$. The coherence length is $X_c = 2 \cdot d_1 = 1.22\frac{\lambda R}{S}$. The area of high contrast in the imaging plane is

$$z_{max} = \frac{\rho}{f}X_c, \tag{2.12}$$

where ρ denotes the diameter of the aperture and f refers to the focal length in the 4f system [25]. This is the area where the interference patterns are visible. Outside of this area, the visibility of the interference pattern is greatly reduced.

3 Methods

3.1 Numerical Methods for the Object - and 4f Simulation

In this chapter, I carry out simulations of the 4f setup using the mathematical framework of Chapter 2. The purpose of this chapter is to present the implementation of the object and the numerical methods used to calculate the wave field. I also introduce a method for calculating the size of simulated speckle and demonstrate its applicability.

Discrete Modelling and Sampling Sizes

In order to allow a numerical calculation of the wave field in the imaging plane, I work with discrete representations of the continuous definitions given in the last chapter. In discrete modelling, the continuous argument **x** is replaced by a discrete counterpart, followed by the replacement of all other continuous functions with their respective discrete representations. This assumes a pixelated wave field, where quadratic pixels of size $\Delta x \times \Delta x$ and $\Delta v \times \Delta v$ are invariant [26]. I calculate the Fourier transform of such distributions with a 2D fast Fourier transform (fft2). The pixels of the fft2 are spaced with $\Delta \xi = 1/(N\Delta x)$, where N is the number of pixels in each direction (a square matrix is assumed). In order to achieve a physically accurate representation of the transformed wave field, the Fourier transform is scaled by a factor of (λf) (according to Equation 2.9). This is indicated in Figure 3.1, where the relationship between the sampling in the imaging plane and the Fourier plane is shown. Since the modulation with
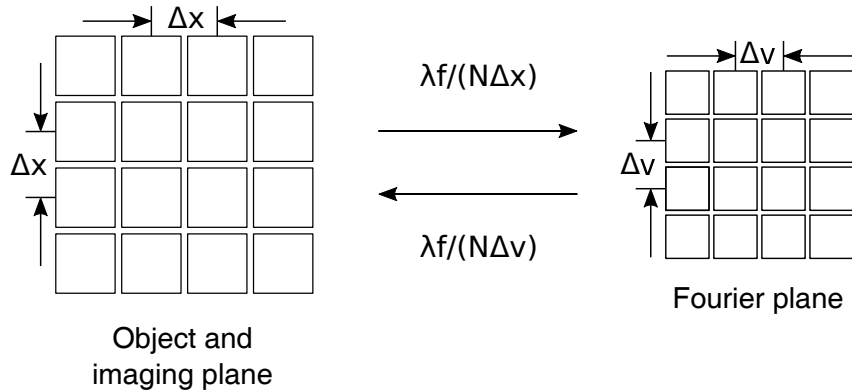

Figure 3.1: Sampling rates in the input plane, Fourier plane and imaging plane. The pixel size in the imaging and sensor plane Δx and in the Fourier plane Δv are related by $\Delta v = \lambda f/(N\Delta x)$. Adapted from [27].

the transfer function H_z is experimentally implemented with a pixelated display spatial light modulator (SLM), the phase modulation by the SLM can be represented very accurately as a matrix with a sampling rate of pixel pitch Δv_{SLM}. It seems reasonable to assume equal pixel size for both the transfer function and the incident wave field on the Fourier plane. This allows the computation of Equation (2.8) by simple element-wise multiplication. The sampling in the input plane is accordingly set to

$$\Delta x = \lambda f/(N\Delta v_{SLM}). \tag{3.1}$$

The sampling rate in the input plane therefore depends on the focal length in the 4f setup and the wavelength of light. This makes the implementation of a light field with multiple wavelengths especially challenging because the wave field in the imaging plane cannot be calculated by a simple matrix addition. The different sampling sizes require a sampling conversion, which produces unwanted artifacts in the output of the simulation.

Integration of a Rough Surface into the Simulation

To simulate the light reflected by the object, I integrated the objects' surface into the simulation. The micro structure of the objects' surface can be represented by a number of randomly distributed points. The distribution in x- and y-direction is uniform, while the points are distributed normally in z. Each of these points is then assumed to be a scattering point, where one spherical light wave originates. This approach to a physical simulation of a speckle field has been taken by Duncan et al. in [28]. The locations were determined at the start of the simulation with coherent light, after that all data was derived from this one object. The superposition of the waves in the input plane at distance z_0 is taken as the input $u_a(\boldsymbol{x_a})$ to the 4f encoding system, as shown in Figure 3.2.
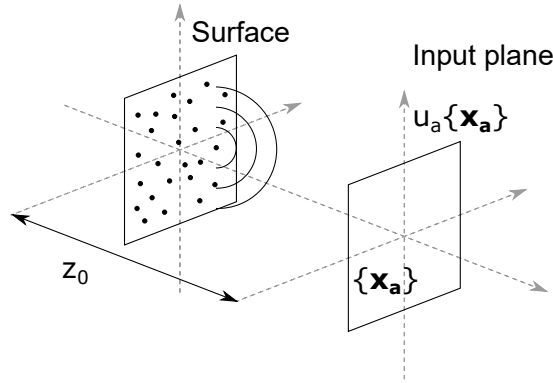

Figure 3.2: Object surface and input plane of the 4f system. The object is represented by a number of spherical waves originating from a surface at distance z_0 from the input plane $u_a(\vec{x_a})$.

I calculate the wavefield in the sensor plane with Equation 2.8. The Fourier transformed wavefield in the input plane U_a is multiplied by the transfer function H_z as well as a circular aperture function A_ρ of diameter ρ, that acts as a low pass filter:

$$u_b = \mathcal{F}^{-1}\{U_b\} = \mathcal{F}^{-1}\{U_a \cdot H_z \cdot A_\rho\}. \tag{3.2}$$

This approach will produce a coherent monochromatic wavefield representation, where depth discrimination is not possible. However, the coherent wavefield produced by rough surfaces have been studied extensively [24, 27], and an analysis of the simulated coherent wavefield can give an indication for the general applicability of the simulation. I also study the speckle size for fully coherent illumination and assume that the results carry over to partially coherent illumination. This is due to the heavily increased computation time.

Speckle Size Estimation with Cross Correlation

In my analysis of the simulated speckle fields, I observe changes in the size of the speckle. One way to quantify and interpret changes in the speckle field is to examine the correlation [28]. I look at the distance Δs it takes for the cross-correlation coefficient c to fall from 1 to 0.5 . The process is illustrated in Figure 3.3.
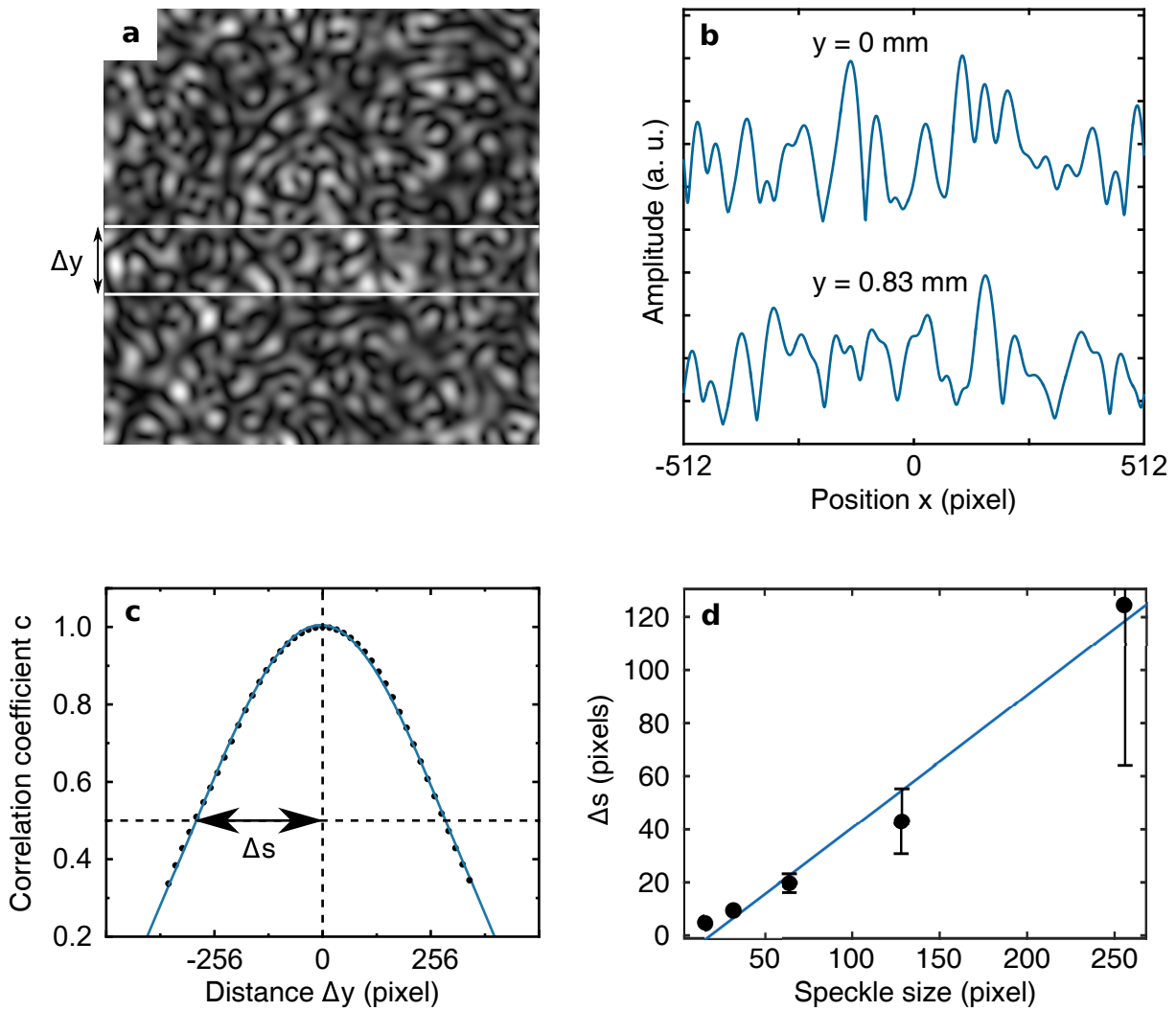
Figure 3.3: Computational speckle size estimation with cross correlation. a, Amplitude distribution of a simulated objective speckle field simulated with known speckle size and two slices indicated in white. **b**, The signal from the two amplitude slices shifted apart vertically for better visibility. **c**, Cross correlation between horizontal amplitude slices Δy pixels apart with the half width at half maximum indicated by Δs. **d**, Parameter Δs plotted over the size of the speckle. Computation of ten random speckle fields for each data point. Error bars indicate standard deviation intervals. A linear relationship can be observed. Δs is proportional to the Speckle size with a factor of (0.5 ± 0.1).

I estimate the similarity of two signals separated by a distance of Δy by calculating their cross correlation. The cross correlation coefficient c is then plotted over Δy. The behavior of the data close to the peak can be approximated by a Gaussian curve. The half width at half maximum Δs of the Gaussian is taken as indicator of speckle size. In order to test the algorithm, I generate speckle fields with a known speckle size. The algorithm for the generation of these speckle fields is based on an algorithm by Duncan et al. [28], where no assumption about the origin of the speckle is made. Here I demonstrate that the parameter Δs computed by my algorithms is directly proportional to the speckle size. The proportionality constant is ≈ 0.5. Δs can therefore be taken as a measure of speckle size. Since my analysis in this work is only concerned with relative sizes, the term "speckle size" is used synonymously with the distance Δs from here on.

Coherence Approximation in the Imaging Plane

When considering partially coherent wavefields, I do not examine the superposition of the spherical waves in the input plane u_a of the 4f system, but in the output plane u_b. This ensures a physically accurate propagation because both amplitude and phase of each of the wavefields can be taken into account when calculating intensity distributions. While the coherence function in the input plane can be described by Equation 2.11, an exact equation for the coherence function in the imaging plane is harder to come by. I approximate the coherence parameter $|\gamma|$ in the imaging plane on the basis of Equation 2.12 and Equation 2.11, where d is the distance between the object and the focal plane. The coherence function in the imaging plane is stretched/compressed by a factor of ρ/f compared to the input plane.

3.2 Experimental Setup of the 4f Imaging System

After showing some of my numerical results in the previous chapter, I present the experimental evidence in Chapter 4.2. The experiment closely resembles the theoretical description in Chapter 2. A detailed depiction of the experimental setup is presented in Figure 3.4.
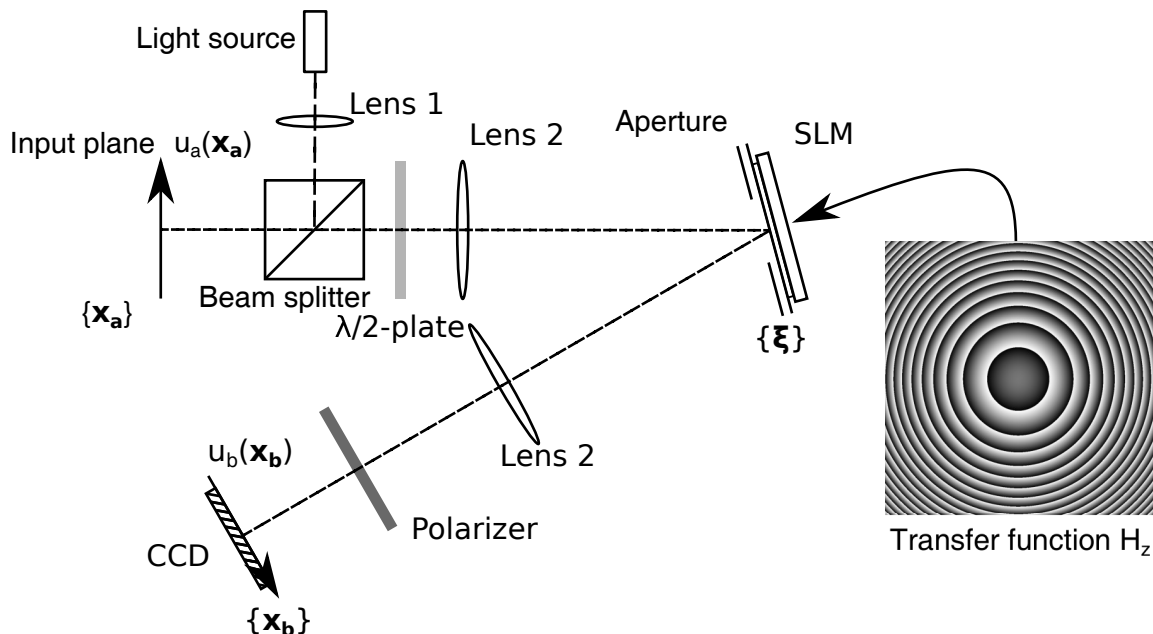

Figure 3.4: Experimental 4f setup with light source, SLM and aperture. The object is illuminated with parallel light from a light source behind lens 1, and is incorporated via beam splitter. The lenses 2 make up the 4f setup. A reflective liquid crystal phase-only spacial light modulator (SLM) in the common Fourier plane manipulates the light. The aperture acts as a low pass filter. The $\lambda/2$-plate and the polarizer ensure that only the modulated component of the light is projected on the sensor CCD. The grey image on the right shows the phase of a transfer function H_z for $z = 5\,\text{mm}$ and $\lambda = 530\,\text{nm}$ that could be inscribed on the SLM.

The object used in the experiments is a metal cylinder with steps of size between 1 μm and 20 μm. I measured the objects' step heights and surface properties in a confocal microscope as a reference (see Appendix Figure A.1).

The light source is incorporated into the setup via an optical fiber of opening diameter S. The focal length of a lens (or the effective focal length of the collimator) in front of the fiber opening are taken as effective distances R between the object and the light source. A beam splitter at $45°$ towards both the object and the lens/collimator ensures perpendicular illumination of the object. A reflective spatial light modulator (SLM) is placed at an angle in the common Fourier

plane of the lenses. To address the SLM, I wrote a program with a graphical interface that writes the transfer function H_z directly on the modulator (see Appendix Figure A.2). I also wrote a program to measure and compensate the misalignment between the two optical axes of the 4f setup and the SLM. The algorithm is based on a paper by Agour et al. [29]. The aperture that I placed directly in front of the SLM acts as a low pass filter towards the incident light. After the manipulation with the SLM and the Fourier aperture, the light is directed through the second lens and onto the CCD of the recording camera. The phase and intensity distributions across the sensor plane u_b then closely resemble the wavefield at distance z from the input plane, thus allowing for depth scans without the need for any mechanical movement in the setup.

4 Results

4.1 Results on Speckle size and Partially Coherent Illumination in the Simulation

Using the methodology described in section 3.1, I calculate coherent and partially coherent wavefields in the imaging plane of the 4f setup. The numerical calculation allows a precise assessment of speckle size and contrast of partially coherent wavefields. The results are also taken into account in the design of the experimental setup.

Amplitude and Phase of Simulated Speckle

I present the amplitude and phase of a wavefield calculated by my algorithm in Figure 4.1. The characteristic speckle pattern is produced by this algorithm as the amplitude. The calculated phase distribution displays the known properties of a speckle wavefield as well. Phase singularities and phase jumps can be seen throughout the phase distribution.
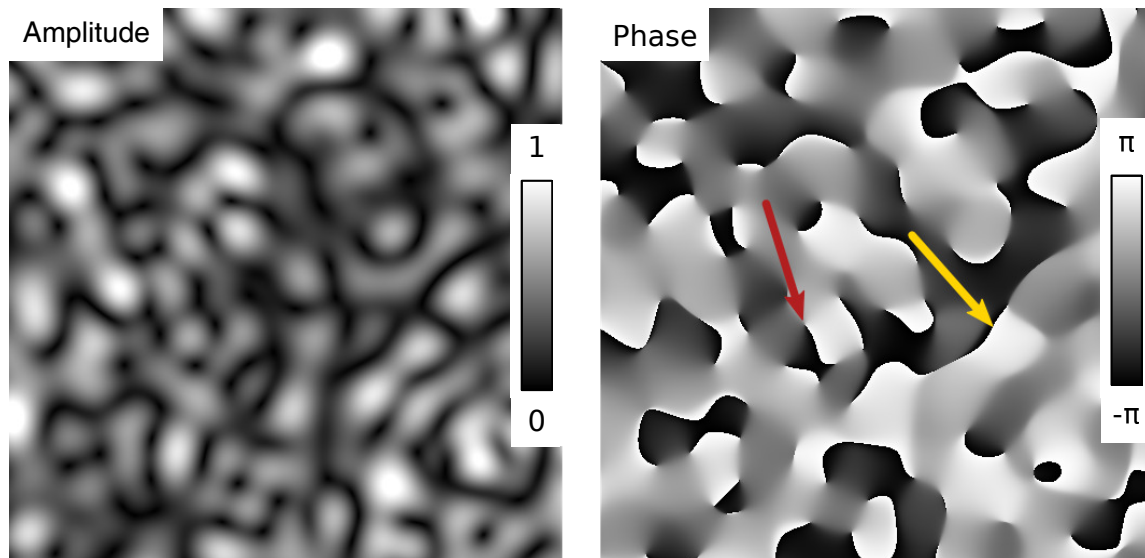

Figure 4.1: Amplitude and phase of numerically simulated coherent speckle wavefield in the sensor plane. The amplitude consists of the characteristic speckle pattern. The phase distribution shows phase singularities (e.g. red arrow) and phase jumps (e.g. yellow arrow). I generated the wavefield with 128 scattering points on a square surface of size 5.42 mm × 5.42 mm, 10 mm from the input plane, illuminated with a wavelength of λ = 530 nm. The 4f setup consists of two f = 100 mm lenses and a Fourier aperture of diameter ρ = 0.25 mm. The sampled area shown is 512 × 512 pixels with a pixel pitch of Δx = 5.2 μm. Presentation adapted from [27].

I am also able to calculate speckle representations at distance z towards the imaging plane by changing the transfer function H_z accordingly. A cross section can be assembled by arranging slices of the amplitude distribution at different z next to each other [27]. In Figure 4.2, one calculated cross section is presented. All amplitude slices were produced starting from the same 128 scattering points.
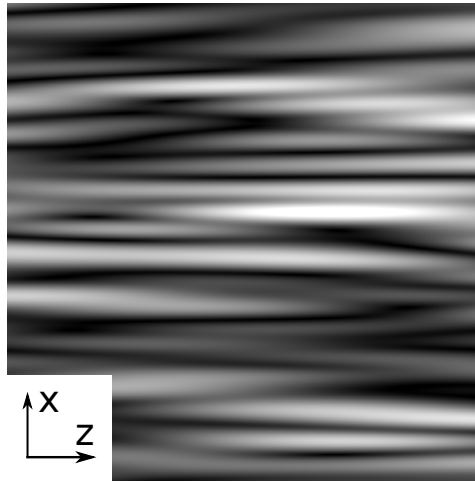
Figure 4.2: Cross section of the amplitude from the generated speckle field. I captured the intensities at different *z* by varying the transfer function H_z in the Fourier domain from *z* = -500 mm to *z* = 500 mm. I generated the wavefield with the same parameters as Figure 4.1. The sampled area shown is 1024 × 1024 pixels. Presentation adapted from [27].

The cigar-like appearance of the speckle becomes apparent. The amplitude distributions are correlated and changes in the amplitude are gradual.

Intensity Histogram of Simulated Speckle

Moving to a quantitative analysis of the data shown in Figure 4.2, I calculate the intensity distribution of the wavefield, shown in Figure 4.3.
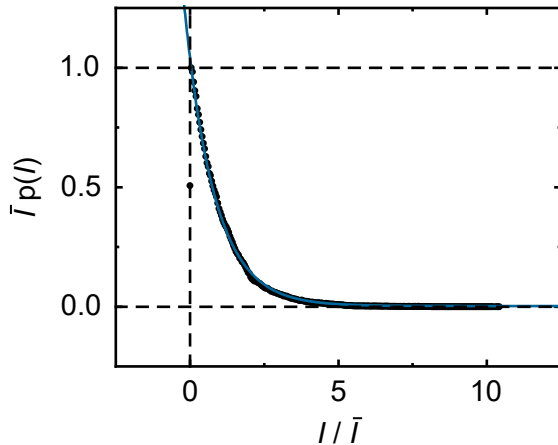

Figure 4.3: Normalized intensity histogram of the calculated coherent speckle pattern. An exponential function $f(I/\bar{I}) = a/\bar{I} \exp(b \cdot I/\bar{I})$ (blue line) is fitted to the data (black dots). The parameters $a \approx 1.01$ and $b \approx -1.02$ were determined. Both are very close to the expected values $a = 1$ and b = -1. The position of the data point at $I/\bar{I} = 0$ is an artifact of the histogram calculation algorithm. The data point is excluded from the fit calculation.

The exponential function $f(I) = 1.01/\bar{I} \exp(-1.02 I/\bar{I})$ is fitted against the data points. The position of the data point at $I/\bar{I} = 0$ is an artifact of the histogram calculation algorithm. The bin for this data point includes values from -1/256 until 1/256. Since no negative intensities can exist, only half the bin is filled with values, which results in a probability density of 0.5 instead of 1. The data point was therefore excluded from the fit calculation.

Size of Simulated Speckle

Another property of interest is the speckle size. I analyze the behavior of the speckle size Δs under a variance in aperture size ρ, wavelength λ and focal length f. I collect all data from the same 128 scattering points and present the results of this analysis in Figure 4.4.
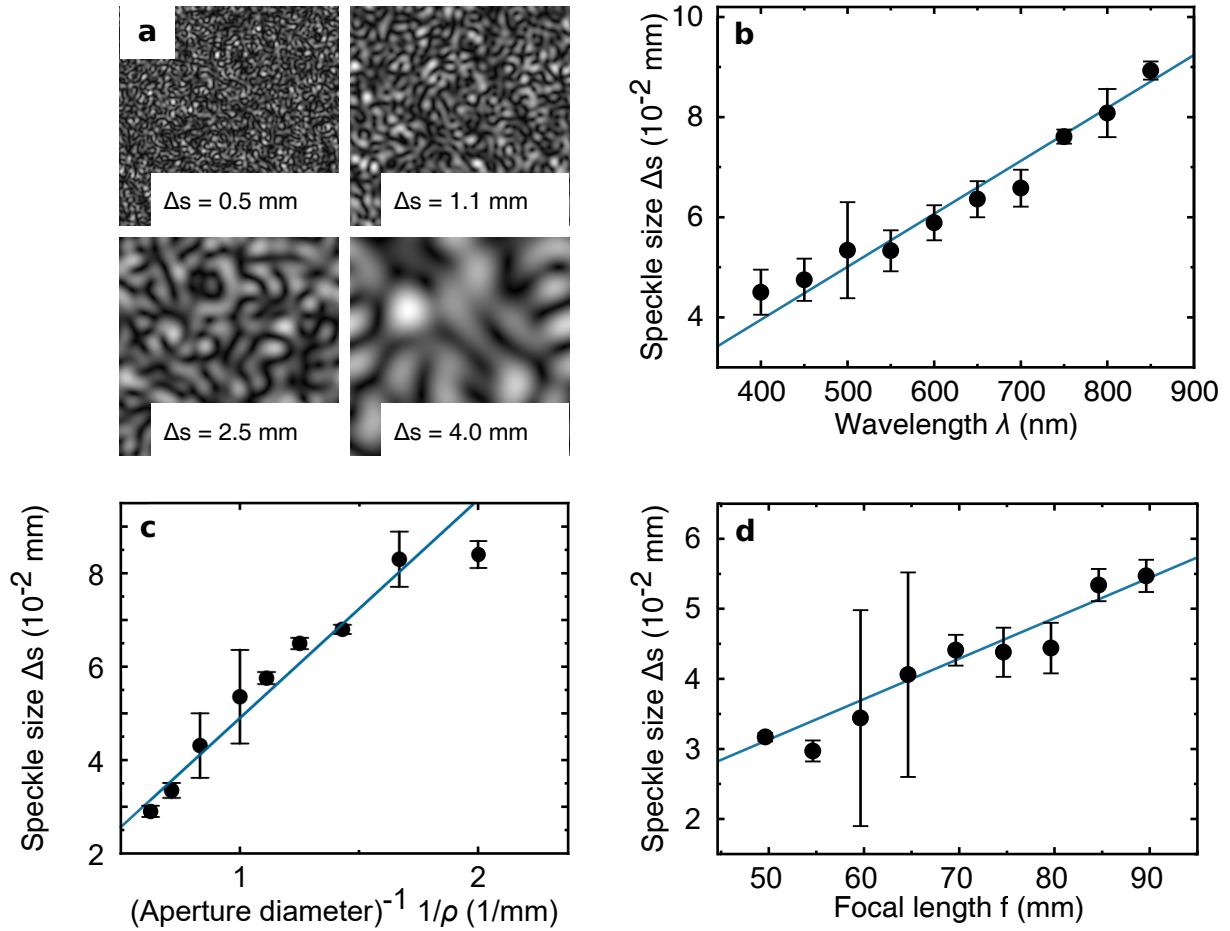
Figure 4.4: Speckle size dependence on wavelength, aperture diameter and focal length in the 4f setup. a, Amplitude distributions of speckle fields with different speckle sizes. **b**, **c**, **d**, Speckle size Δs plotted over the wavelength of light λ, the reciprocal of aperture diameter $1/\rho$ and focal length f, respectively. Linear curves were fitted against the data. Error bars indicate 95% confidence intervals. Linear relationships can be observed in all three cases. (units)

I computed all data points from the same 128 scattering points. The size of the Fourier aperture is inversely proportional to the speckle size Δs, while wavelength and focal length are directly proportional to the speckle size.

Contrast in Simulated Partially Coherent Speckle

After accessing coherent wavefields produced by the algorithm, I extend the simulation to include a spatial coherence function. Using this altered algorithm, I am able to simulate partially coherent wavefields. One particular example is presented in Figure 4.5, where I place the surface at a distance of $z_0 = 10$ mm from the imaging plane. Using the transfer function H_z inscribed in the SLM, I look at amplitude distributions close to the location of the surface. The focal length of the 4f setup is $f = 150$ mm and the diameter of the aperture is set to $\rho = 1$ mm.

z = 10 mm   z = 9.5 mm   z = 9 mm   z = 8.5 mm
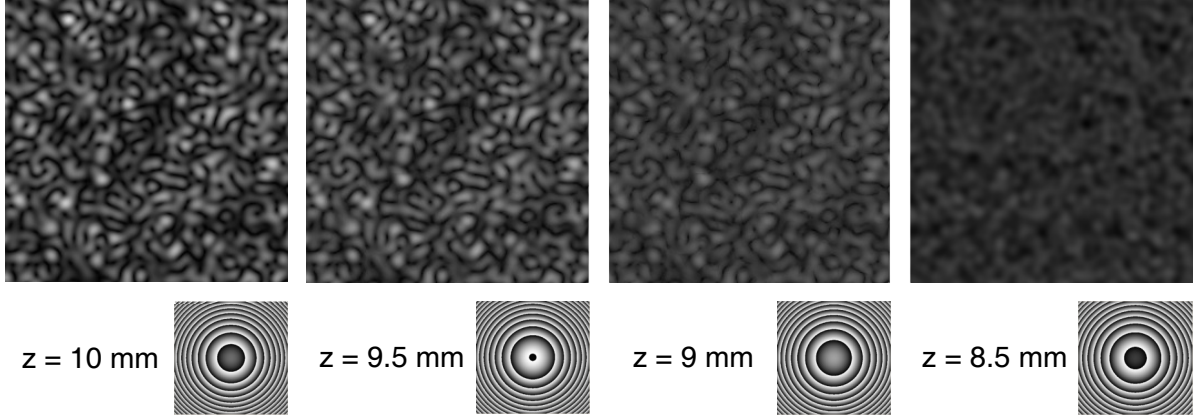
Figure 4.5: Numerically calculated amplitude distributions of a partially coherent wavefield at different propagation distances. I placed the objects' surface at $z_0 = 10$ mm and scanned through the incoherent wavefield by changing the transfer function H_z on the SLM accordingly. The contrast changes with the distance to the objects' surface. I calculated the amplitude distributions from 1024 scattering points on a square surface of 5.42 mm $\times$ 5.42 mm, 10 mm from the input plane, illuminated with monochromatic light of wavelength $\lambda = 530$ nm. The wavefield was processed through a 4f optical filter with $f = 150$ mm and an aperture diameter of $\rho = 1$ mm. The sampled areas shown are 256 $\times$ 256 pixels with a pixel pitch of $\Delta x \approx 10$ um.

As a result, a drastic change in contrast can be observed. Larger distances to the object correspond to amplitude distributions of lower contrast in the sensor plane of the 4f optical system.

Cross Section of Simulated Partially Coherent Speckle

The change in contrast is visualized in Figure 4.6, where I calculate a cross section of the same wavefield depicted in Figure 4.5 analogous to Figure 4.2. I calculate the contrast values for each of the cross sections separately and plot them against the distance Δz towards the objects surface.

An area of high speckle contrast surrounds the objects' surface. The intensity in direct proximity of the object develops a contrast plateau of width $\approx z_{max}/2$, where the contrast is larger than 0.95. The contrast then falls sharply to a value of 0.6. An area of depth $z_{max} \approx 1.2\,mm$ around the object has a contrast value larger than 0.6. This is consistent with theoretical calculations. By applying Equation 2.11, I estimate the coherence length to about $X_c \approx 0.13\,mm$. Taking Equation 2.12 into account, I can therefore calculate the depth of the area of high contrast to $z_{max} = 1.3\,mm$.
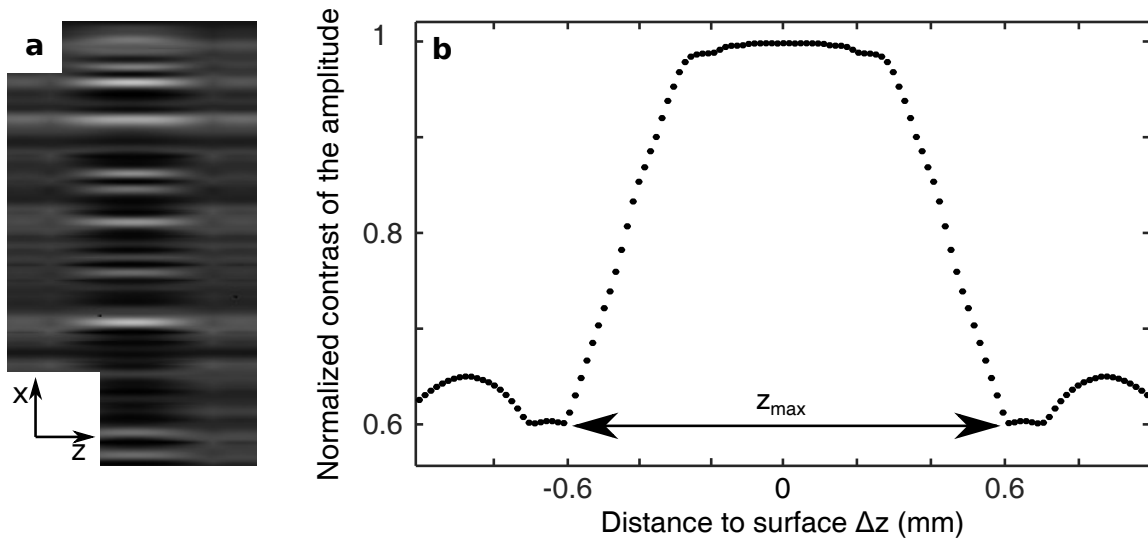
Figure 4.6: Cross section and contrast values of the simulated incoherent amplitude distributions near the objects' surface. a, Cross section of the wavefields' amplitude. The amplitude slices at different z were calculated by varying the transfer function in the Fourier domain from $z = 9\,mm$ to $z = 11\,mm$. The area of high contrast surrounding the objects' surface is clearly identifiable. **b**, Contrast of the partially coherent interference pattern. $z_{max} \approx 1.2\,mm$ denotes the area where the contrast of the recorded intensity distribution is high. normalized Contrast

4.2 Experimental Results on Speckle Size and SLM Propagation

After an extensive theoretical description of the mechanism, I now invite the reader to consider some of the experimental evidence that I am able to obtain. All images shown are intensity distributions of the wavefield that I captured experimentally with a recording camera in the imaging plane of the 4f setup.

Size of Speckle in the Experiment

In the previous chapter, the size of the simulated speckle was examined. I now do the same for my experimental findings. In order to look at the changes in the intensity distribution of the wave field, I used a Helium-Neon Laser (λ = 633) to illuminate the objects' surface. The high spectral purity ensures a clear interference pattern in the sensor plane. In Figure 4.7, such intensity distributions are shown. I varied the size of the aperture in front of the spatial light modulator (SLM) in the Fourier plane between $\rho \approx 2$ mm and $\rho \approx 6$ mm. The fiber opening (S = 200 μm) is coupled in a collimator with effective focal length R = 18 mm. The focal length in the 4f setup is f = 100 mm.

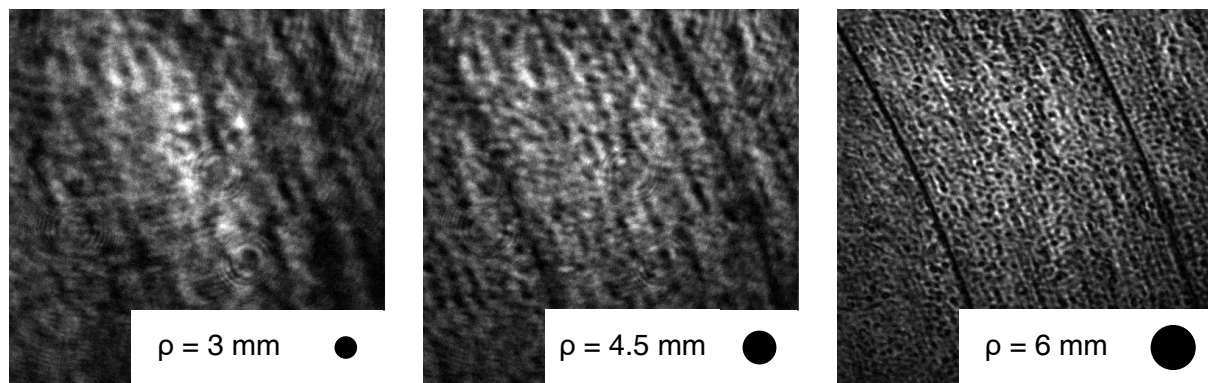ρ = 3 mm ● ρ = 4.5 mm ● ρ = 6 mm ●

Figure 4.7: Influence of the aperture diameter in the Fourier plane on the intensity distribution in the experiment. The speckle become smaller as the aperture opens up. I illuminate the object with a Helium-Neon-Laser (λ = 633 nm) that is coupled over a S = 200 μm optical fiber in a collimator of effective focal length R = 18 mm. The lenses in the 4f setup were of focal length f = 100 mm. The images captured are 512 × 512 pixels and 1.8 mm × 1.8 mm. Circles indicating aperture size not to scale.

I observe the shift in speckle size predicted by my algorithm (see Figure 4.4) in the experiment as well. A larger Fourier aperture leads to smaller speckle, and vice versa. The intensity distributions captured for smaller aperture sizes also experience an apparent reduction in image sharpness. The two dark curved lines from top to bottom are steps in the objects' surface. The spatial coherence length for this setup can be calculated according to Equation 2.11 and amounts to a value of $X_c \approx 69.5$ um. The steps visible in the images are the steps no. 9 and 10, which are 10 um and 20 um high (for reference see Appendix Figure A.1). Owing to the high spatial coherence, no difference in contrast can be observed throughout one captured intensity.

SLM Propagation in the Experiment

While the spatial and temporal coherence length in the setup examined in the previous section was relatively high, I now use a 530 nm LED with a larger fiber opening of S = 400 μm and adjust the effective focal length of the collimator to R = 6 mm to arrive at a coherence length of $X_c \approx 8$ μm, accoding to Equation 2.11. I hypothesize that objects in focus have a much higher

contrast compared to objects further away from the focal plane. Using this setup, I demonstrate that by writing the appropriate transfer function H_z onto the SLM, I can shift the focal plane to a location at distance z from the input plane. This process is illustrated in Figure 4.8.
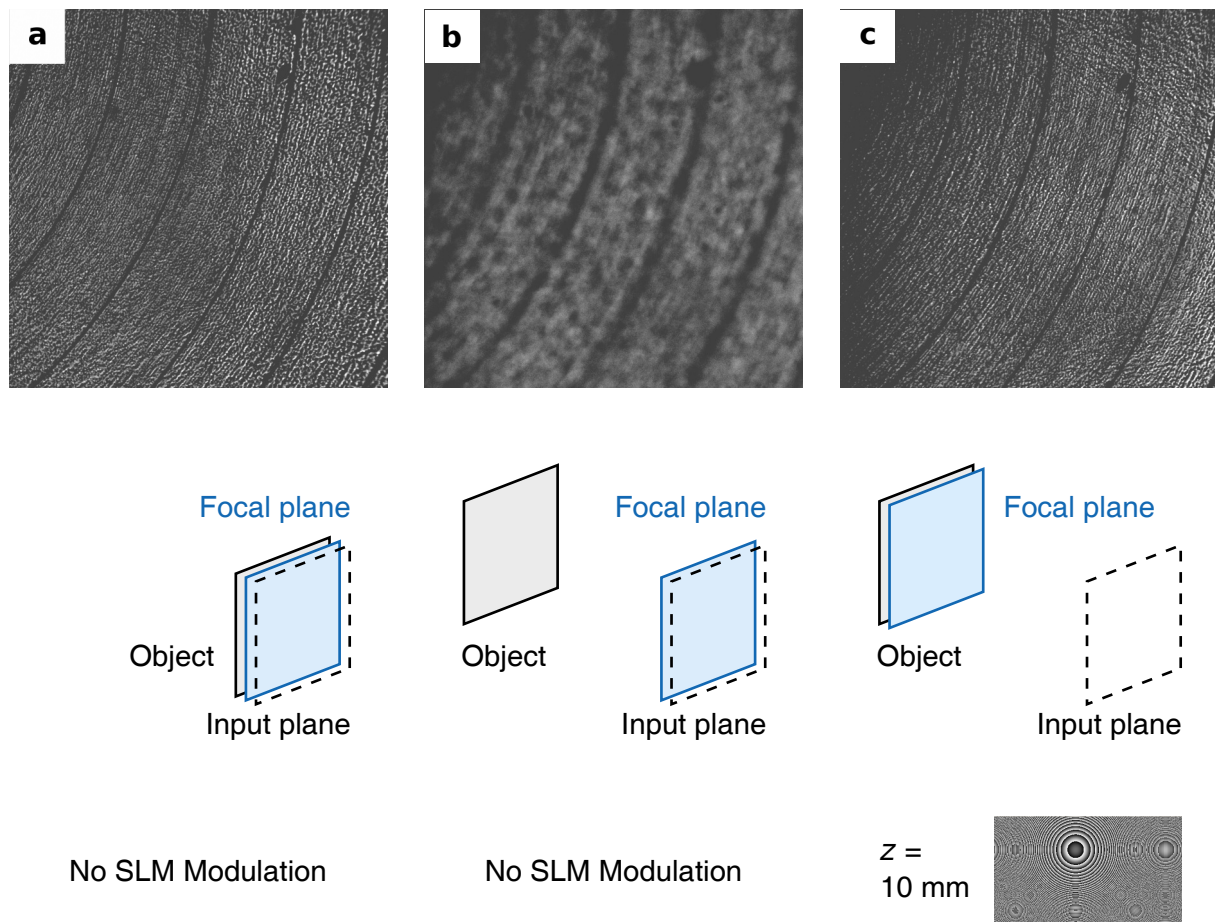
Figure 4.8: Moving the focal plane via SLM. a, Sharp image of the object in the input plane of the 4f setup with no SLM modulation. **b**, Blurred image of the object at distance $z_0 \approx 10\,\text{mm}$ from the input plane with no SLM modulation. **c**, Sharp image of the object at distance $z_0 \approx 10\,\text{mm}$ from the imaging plane with the SLM shifting the focal plane to $z = 10\,\text{mm}$. The reduction of brightness on the left side is owed to the fact that the light source is further away from the object compared to image **a**.

An object out of focus can be brought into focus by changing the transfer function H_z on the SLM. No difference in image sharpness or speckle size can be observed between different positions of the focal plane, given that the object is in focus. This is true up to a distance of at least 10 mm, as demonstrated by my experiment.

Contrast Difference for Surface Features Under Partially Coherent Illumination in the Experiment

To improve the visible contrast difference in the objects' surface, I use illumination with a shorter coherence length compared to the previous section. I use an optical fiber with an opening diameter of $S = 1.4$ mm to connect the $\lambda = 530$ nm LED, but keep the effective focal length of the collimator at $R = 6$ mm. The focal length of the lenses in the 4f setup is $f = 100$ mm and the aperture is set to about $\rho \approx 6$ mm. I calculate the depth of high contrast to $z_{max} \approx 55$ µm. The images taken in this setup are presented in Figure 4.9.

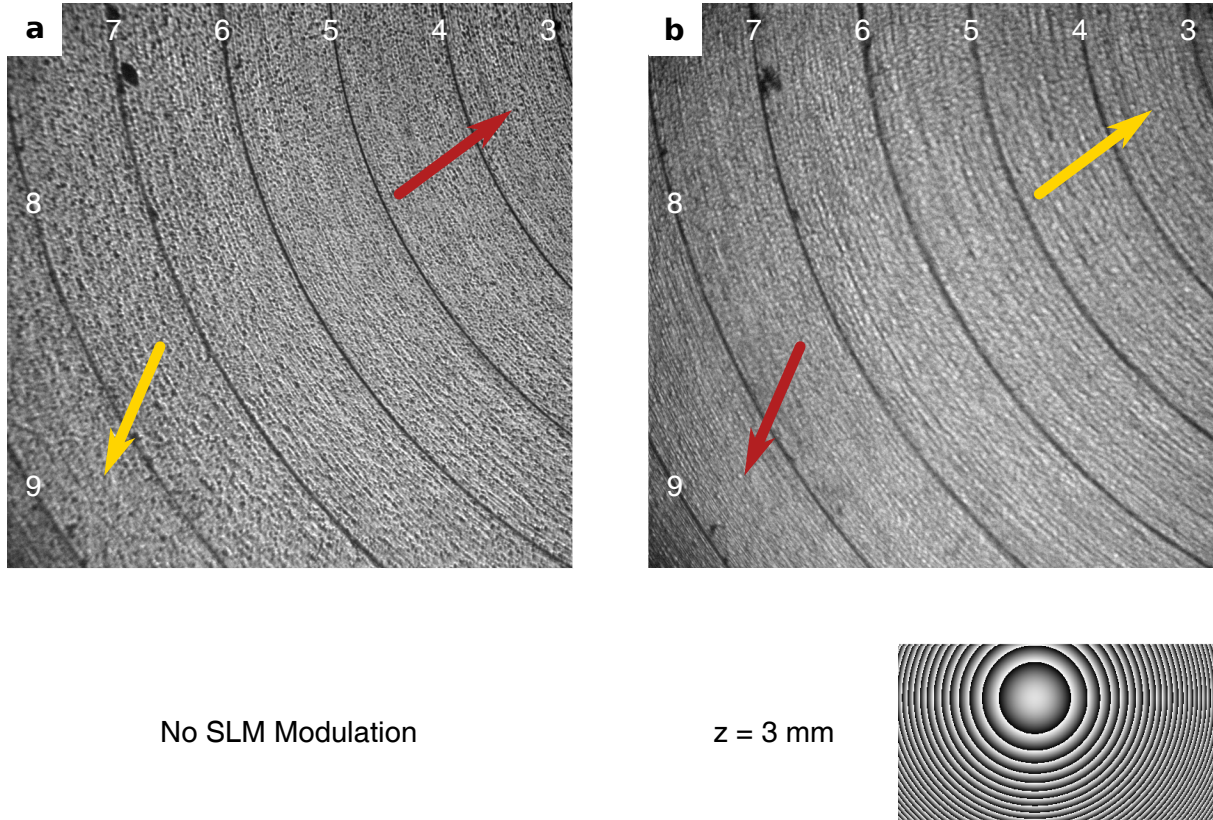No SLM Modulation   z = 3 mm

Figure 4.9: Sharpness difference between steps in the surface at partially coherent illumination. Numbers in white referring to step number, see Appendix Figure A.1. Red arrows indicating area in focus, yellow arrows indicating area out of focus. The combined height of steps 4-8 adds up to 35 µm. **a**, Intensity distribution captured without SLM modulation. **b**, A transfer function Hz for $z = 3$ mm is written on the SLM. This results in a shift of the focal plane closer to the outermost ring. The parameters of the setup were set to: fiber opening diameter $S = 1.4$ mm, effective collimator focal length $R = 6$ mm, wavelength of light $\lambda = 530$ nm, 4f focal length $f = 100$ mm and aperture diameter $\rho \approx 6$ mm

A difference in contrast can be made out from the left most step to the right most visible step, although the effect is relatively small compared to Fig. 4.8. Since the depth of high contrast is $z_{max} \approx 55$ µm and the height difference is only 35 µm. The contrast reduction is small, because the transfer function only propagates towards the edge of the falling slope of the coherence function (as shown in Figure 4.6).

5 Discussion: Development of the Measuring Method

I discuss all simulated and experimental evidence presented in the previous two chapters. I evaluate the physical accuracy and applicability of the simulated results and interpret them with regard to the experiment. Furthermore, I analyze the experimental data considering the development of a measuring method.

Physical Accuracy of the Simulated Coherent Speckle Fields

The simulation that I developed in the course of this work produces accurate relative representations of monochromatic, coherent speckle fields. This is indicated by the appearance of the amplitude and phase distributions in Figure 4.1 and Figure 4.2. They closely resemble earlier simulations by Agour in [27] and experiments by Goodman in [30]. Goodman's description of the intensity distribution fits my description almost exactly. Since energy conservation is not considered in my algorithm, only relative intensity and amplitude comparisons across one calculated image can be made. The investigation of speckle size and contrast comply with this procedure.

Explanation for the Speckle Size Dependence

Schnars et. al. describe the subjective speckle size in [24], although the description is limited to a simpler setup. In my analysis, I take a novel approach for the size measurement of simulated speckle and assume that the correlation distance Δs is related to the size of the speckle. I perform a series of tests, which are discussed in greater detail in chapter 3.1, where I demonstrate the proportionality between speckle size and Δs. According to my results in section 4.1, the Speckle size Δs is related to wavelength, aperture size and focal length by the proportionality

$$\Delta s \propto \frac{\lambda f}{\rho}. \tag{5.1}$$

Since the aperture in the Fourier plane acts as a low pass filter, the inverse proportionality with the size of the low pass filter ρ is expected. Including higher frequencies inevitably leads to smaller speckles. The dependence on the wavelength λ and focal length f is a result of the Fourier transforming property of lenses described by Equation 2.9. A change in focal length f or wavelength λ leads to a different spacing of the frequencies in the Fourier plane. Assume ξ_{max} to be the largest frequency included in the aperture, so that

$$\xi_{max} \propto \rho/(\lambda f). \tag{5.2}$$

Although the physical aperture size ρ stays constant, a change of λ or f leads to a different sized low pass filter ξ_{max} and thereby changes the speckle size. The measured results were obtained from a simulation using one object as starting point for all calculations. Considering this, one could argue that the data points are not distributed as close to the fitted functions as one might expect. The calculations are, albeit not random, very chaotic. A small change in the frequency domain leads to a drastically different distribution in the imaging plane. This explains the deviations. The large error bars are confidence intervals from the Gaussian fit and attribute to the fact that the data did not always follow a perfect normal distribution.

Implications of the Simulated Results for the Image Quality in the Experiment

The model predictions strongly suggest an influence of wavelength, aperture size and focal length in the 4f setup on the size of the speckle. This is important, because small speckle might not be accurately resolved by the CCD of the recording camera and thus lead to contrast reduction. Larger speckle might reduce the resolution of the contrast measurement in the transversal axes. The minimum area needed for accurate contrast evaluations might be greater for larger speckle.

Implications of the Simulated Results for the Geometry of the Experimental Setup and the Parameters of the Light Source

My numerical calculations of partially coherent speckle fields deliver amplitude distributions that are high in contrast when the objects' surface is in focus and low in contrast, when the objects surface is out of focus. These findings are in good agreement with the theoretical description given in Chapter 2. In order to achieve a high measuring accuracy in the lateral axis, z_{max} should be as low as possible. Since the opening of the Fourier aperture affects both the speckle size and the depth of field, a trade off between large speckle and a small depth of field has to be made. The focal length of the lenses used in the 4f setup should be set to a value as small as possible. However, since a reflective spatial light modulator (SLM) is used in the setup, geometric restrictions have to be considered. The wavelength of the light source should also be minimized, although the optical equipment used in the experiment such as the $\lambda/2$-plate, camera and SLM are optimized for visible light. A wavelength of 530 nm is therefore a reasonable compromise between minimizing the spatial coherence length and measuring effectively. The distance between object and light source should be minimized, while the opening size of the fiber cable should me maximized in order to minimize the spatial coherence length. It should be noted that a small spatial coherence length is desirable, but having too little spatial coherence can cause the interference pattern to disappear altogether.

Limited Application of the Simulated Results

Please also note that I obtain all simulated data for one wavelength, meaning that the simulated light source is assumed to be monochromatic and of infinite temporal coherence length. In contrast, LEDs often have temporal coherence lengths in the micrometer range. It is therefore important to realize that the results do not necessarily represent a speckle field produced by an LED. A polychromatic wave field can not be simulated by a simple superposition of monochromatic wavefields. A change in wavelength also results in a small difference in the frequency spacing at the Fourier plane. In my simulation, this change results in an altered sampling rate, so that the combination of the wavefields necessarily include sampling conversion, which introduce several unwanted artifacts. This could be circumvented in part by setting a higher sampling rate. A higher sampling rate in the imaging plane leads to a lower sampling rate in the Fourier plane and vice versa. For my calculations, the sampling rates were in the same order of magnitude, but an imbalance could lead to even more inaccuracies. Another problem is the much slower computation rate, which scales approximately with the square of the sampling rate.

Speckle can be observed experimentally as a product of LED illumination. The representation of an LED spectrum as single wavelength is a close approximation, ignoring the effects of temporal coherence. The treatment of the light source as monochromatic is therefore a close approximation of the behavior under LED illumination. Especially the results concerning the speckle size should be universal in this regard.

Impact of Speckle Size on Image Quality in the Experiment

The experimental data I was able to obtain on speckle size is in line with the simulated results. As expected, a larger aperture size leads to smaller speckle and vice versa. Using the Helium-Neon laser, I did not observe any reduction in contrast for minimally sized speckle. However, looking at the largest speckle, I noticed a reduction in sharpness and overall quality of the image. This could be in part due to the reduced area of maximum contrast z_{max} because of the smaller aperture. Another possible explanation lies in the nature of the speckle themselves. Surface features smaller than the smallest speckle simply can not be resolved if speckle are seen throughout the image.

SLM Propagation in the Experiment

The experimental implementation of the transfer function of propagation via SLM works as expected. My experimental findings are in line with my simulated results. The focal plane can be shifted to a location at distance z towards the input plane. This method produces propagated intensity distributions of wavefields that are indistinguishable from the actual intensities at the propagation distances. The simple experimental setup used in the course of this work can provide these as output for distances up to 10 mm. This number looks very promising in the context of micro parts. Further research is needed to determine factors that influence this maximum propagation distance.

Inconsistencies of Height Differences with the Transfer Function and Insufficient Contrast Change

The changes in contrast and sharpness in the experimental investigation are comparable to the predictions made by the model. The surface features of the object are not pronounced enough to see a significant difference in contrast. The transfer function written on the SLM was not consistent with the height difference. One contribution to this inconsistency could be an inaccurate adjustment of the object, so that it is not exactly perpendicular to the optical axis. However, the transfer function does not function well for small propagation distances. Almost no change in the wavefield can be observed. More research is needed on this topic. The short spatial coherence length had the effect that it contributed to a suppression of speckle formation. In order to realize smaller depths of field, a microscope objective could be mounted in front of the 4f setup. This would allow better speckle visibility, because a longer spatial coherence length is possible, while simultaneously providing a depth of field that is much more shallow. Another obvious benefit is a higher sampling rate in the transversal axes due to the magnification of the microscope objective. This is a preferable outcome regardless, since the application of the method is concerned with micro parts.

6 Conclusion and Outlook

In the course of this work I investigated several aspects of a 4f setup with a spatial light modulator in the Fourier plane. The spatial light modulator was instructed to display a phase shifting transfer function of propagation. I studied the effect of the wavelength of light, the opening diameter of the light source, the distance of the light source, as well as the focal length and the size of the Fourier aperture. For coherent illumination, the size of the Speckle is affected (Figure 4.4, 4.7). For partially coherent illumination, the area, where high contrast interference occurs, is affected as well (Figure 4.6, 4.8).

This was examined both in a numerical simulation that I based off of Fourier optics, and in the experimental system itself, which I set up and took into operation (Chapter 3.2). In order to address the spatial light modulator, I wrote a program that would detect and compensate misalignment between the optical axes and display the appropriate transfer function of propagation onto the device (Appendix A.1).

All three hypotheses proposed in Chapter 1 were investigated, although not all of them could be addressed conclusively.

Hypothesis 1
The first hypothesis could be validated in the simulation and experiment. In my investigation of speckle size I found that the size of the speckle is directly proportional to the focal length and the wavelength of light and inversely proportional to the diameter of the aperture. These results were provided by my numerical simulation and are in good agreement with the general theoretical description. I was also looking at the speckle size dependence in the experiment, where I found supporting evidence that the speckle size is inversely proportional to the aperture size.

Hypothesis 2
The second hypothesis could be fully validated in the experiment, but the experimental results are inconclusive thus far. The speckle produced by partially coherent illumination are found to be of high contrast around the objects' surface and of significantly lower contrast after a distance towards the surface. I found this to be the case in the calculated wavefields and in the experiment. The precise depth of this area could be predicted in the simulation, but the experimental findings were not in line with theoretical predictions.

Hypothesis 3
The third hypothesis is fully validated by both the simulation and the experiment. The propagation using the spatial light modulator with the transfer function of propagation did function as expected. I was able to move the focal plane away from the input plane of the 4f setup without the need for any mechanical movement of the object in and out of focus.

Outlook

While it could be shown that the method exhibits an extended depth of focus and accurate measurements in the micrometer range are possible in the simulation, the accuracy in the experiment was lacking. It is likely that a microscope objective in front of the 4f setup improves the accuracy of the measurements in future experiments.

The setup did not include any high speed components such as a high performance video camera or a digital mirror device. These are crucial for the execution of the proposed measuring method. The extend to which my findings can be translated to such a setup has to be investigated.

The 4f setup is more robust in general because of the common path configuration. This claim has not been quantified thus far and needs to be investigated as well.

Looking at the simulation, an amplitude modulation following the operating principle of the digital mirror device could be implemented in place of the phase-only modulation in order to explore the possibilities and limitations of such a setup.

Finally, depth discrimination measurements on the basis of contrast differences have to be implemented.

References

[1]   U. Schnars and W. Jueptner. "Direct recording of holograms by a ccd target and numerical reconstruction". In: *Applied Optics* 33 (1994), pp. 197–181.

[2]   U. Schnars and W. Jueptner. *Digital Holography*. Springer, 2005.

[3]   T. Kreis. *Holographic Interferometry*. Akademie Verlag, 1996.

[4]   M. Takeda, H. Ina, and S. Kobayshi. "Fourier-transform method of fringe-pattern analysis for computer-based topography and interferometry". In: *Journal of the Optical Society of America* 72 (1982), pp. 156–160.

[5]   U. Schnars and W. Jueptner. "Automatic evaluation of holographic interferograms by reference beam phase shifting". In: *Proceedings of SPIE* 398 (1982), p. 22.

[6]   I. Yamaguchi and T. Zhang. "Phase-shifting digital holography". In: *Optics Letters* 22 (1997), pp. 1268–1270.

[7]   Y. N. Denisyuk. "On the reproduction of the optical properties of an object by the wave field of its scattered radiation II". In: *Optics and Spectroscopy (USSR)* 18 (1965), pp. 152–156.

[8]   E. Leith and R. Hershey. "Transfer functions and spatial filtering in grating interferometers". In: *Applied Optics* 24 (1985), pp. 237–239.

[9]   T. Dresel, G. Häusler, and H. Venzke. "Three-dimensional sensing of rough surfaces by coherence radar". In: *Applied Optics* 18 (1992), pp. 919–1925.

[10] J.C. Wyant. "White light interferometry". In: *Proceedings of SPIE* 4737 (2002), p. 98.

[11] A. F. Fercher. "Ophthalmic interferomety". In: *Proceedings of the International Conference on Optics in Life Sciences, Garmisch-Partenkirchen, Germany, 12–16 August 1990. Eds. G. von Bally and S. Khanna* (1990), pp. 221–228.

[12] D. Huang et al. "Optical coherence tomography". In: *Science* 254 (1991), pp. 1178–81.

[13] P. Pavlícek and G. Häusler. "White-light interferometer with dispersion: an accurate fiber-optic sensor for the measurement of distance". In: *Applied Optics* 44 (1991), pp. 2978–2983.

[14] M. Szkulmowski et al. "Flow velocity estimation using joint Spectral and Time domain Optical Coherence Tomography". In: *Optics Express* 16 (2008), pp. 6008–6025.

[15] M. Hering et al. "Fne-shot line-profiling white light interferometer with spatial phase shift for measuring rough surfaces". In: *Proceedings of SPIE* 6188 (2006), 6188E.

[16] C. McCutchen. "Generalized Source and the van Cittert-Zernike Theorem: A Study of the Spatial Coherence Required for Interferometry". In: *Journal of the Optical Society of America* 56 (1966), pp. 727–732.

[17] J. Biegen. "Determination of the phase change on reflection from two-beam interference". In: *Optics Letters* 19 (1994), pp. 1690–1692.

[18] J. Rosen and A. Yariv. "Longitudinal partial coherence of optical radiation". In: *Optics Communications* 117 (1995), pp. 8–12.

[19] T. Klein et al. "Novel approach for shape measurement using light with low spatial coherence length". In: *TOM 6- Frontiers in Optical Metrology* (2018).

[20] J. W. Goodman. *Introduction to Fourier Optics*. The McGraw Hill Companies, 1968.

[21] G. C. Sherman. "Application of the convolution theorem to Rayleigh's integral formulas". In: *Journal of the Optical Society of America* 57 (1967), pp. 546–547.

References

[22] C. Falldorf et al. "Phase retrieval by means of a spatial light modulator in the Fourier domain of an imaging system". In: *Applied Optics* 49 (2010), pp. 546–547.

[23] M. Agour et al. "Automated compensation of misalignment in phase retrieval based on a spatial light modulator". In: *Applied Optics* 50 (2011), pp. 4779–4787.

[24] U. Schnars et al. *Fundamental Principles of Holography*. Berlin, Heidelberg: Springer Berlin Heidelberg, 2015, pp. 5–38. ISBN: 978-3-662-44693-5. DOI: 10.1007/978-3-662-44693-5_2. URL: https://doi.org/10.1007/978-3-662-44693-5_2.

[25] M. Agour et al. "Measuring the complex amplitude of wave fields by means of phase retrieval using partially coherent illumination". In: *Fringe 2013*. Springer, 2014, pp. 283–287.

[26] V. Katkovnik and J. Astola. "Phase retrieval via spatial light modulator phase modulation in 4f optical setup: numerical inverse imaging with sparse regularization for phase and amplitude". In: *JOSA A* 291 (2012), pp. 105–116.

[27] M. Agour. *Determination of the complex amplitude of monochromatic light from a set of intesity obervations*. Strahltechnik Band 47. BIAS Verlag, 2011.

[28] D. D. Duncan and S. J. Kirkpatrick. "Algorithms for simulation of speckle (laser and otherwise)". In: *Complex Dynamics and Fluctuations in Biomedical Photonics V*. Vol. 6855. International Society for Optics and Photonics. 2008, p. 685505.

[29] M. Agour et al. "Automated compensation of misalignment in phase retrieval based on a spatial light modulator". In: *Applied optics* 5024 (2011), pp. 4779–4787.

[30] J. W. Goodman. "Some fundamental properties of speckle". In: *Journal of the Optical Society of America* 6611 (1976), pp. 1145–1150.

Appendix

A.1 Confocal Microscope Measurement of the Object

In order to get a good idea of the depth of field properties of the imaging system, an object with carefully designed surface properties was constructed. It has 12 steps of different heights between 1 μm and 20 μm. The object can be used for calibration in a wide range of applications. I took the object into a confocal microscope to confirm the height properties. I also measured the surface roughness. The results of this investigation are presented in Appendix Figure A.1.
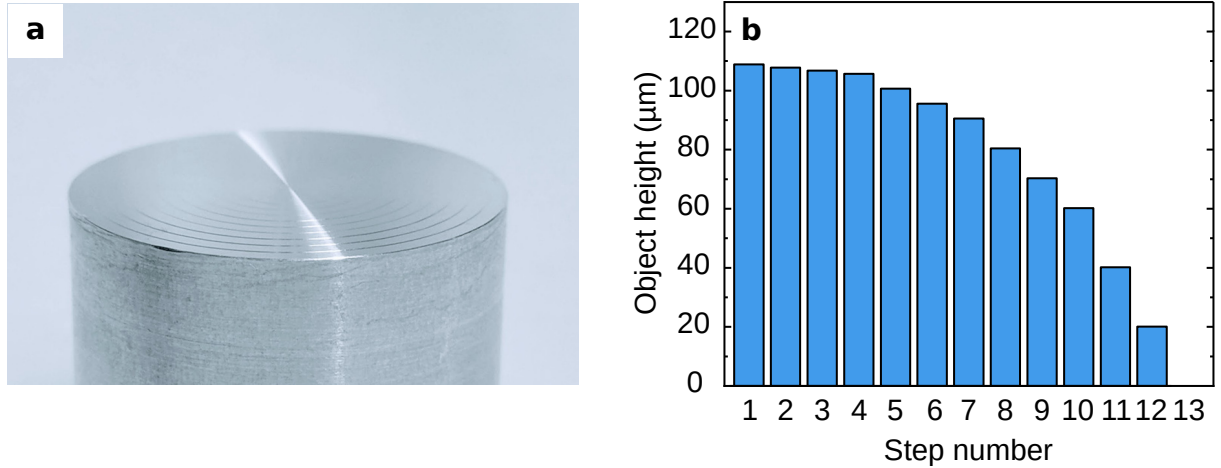
Appendix A.1: The object used in the experiment.
a, Photograph of the object. The concentric rings on top of the object are the steps on the surface. I measured the surface roughness in a confocal microscope. The mean square error of the Gaussian height distribution on a planar ring is $\sigma = 30$ nm. **b**, Height of the object as measured in a confocal microscope. Ring numbers counted from the innermost ring. The surface consists of 13 parallel, planar and concentric ring surfaces of varying height and constant width ≈ 1 mm. **c**, The step height between rings of constant height as measured in a confocal microscope. The surface has four groups of three steps each. The groups have a height of 1 μm, 5 μm, 10 μm and 20 μm, respectively (counted from the innermost ring).
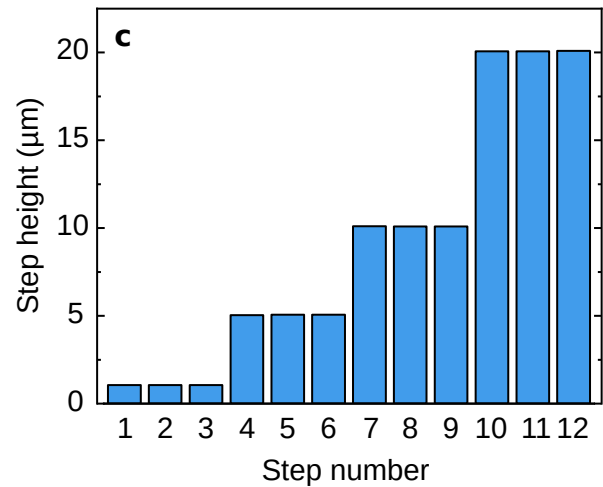
The measured heights of the steps are greater than the expected values. The deviations are smaller than 100 nm in all cases. For the smallest steps of 1 μm, I measure a deviation of 50 um, a 5 % difference. The height histogram of the planar surfaces roughly follow a Gaussian with $\sigma = 30$ nm. The height distribution characterizes the surface roughness of the object. This distribution was integrated in the simulations discussed in Section 3.1 and Section 4.1.

A.2 Controlling the Spatial Light Modulator

In my experiments, the spatial light modulator (SLM) is integrated in the Fourier plane of a 4f setup. It is connected with a computer via Digital Visual Interface (DVI). The computer identifies the device as a secondary monitor of resolution 1920 times 1020 pixels. A greyscale image displayed on the screen is taken as input. A value of 0 in the image corresponds to a phase shift of 0, a value of 255 corresponds to a phase shift of 2π, with all the values inbeween scaled linearly.
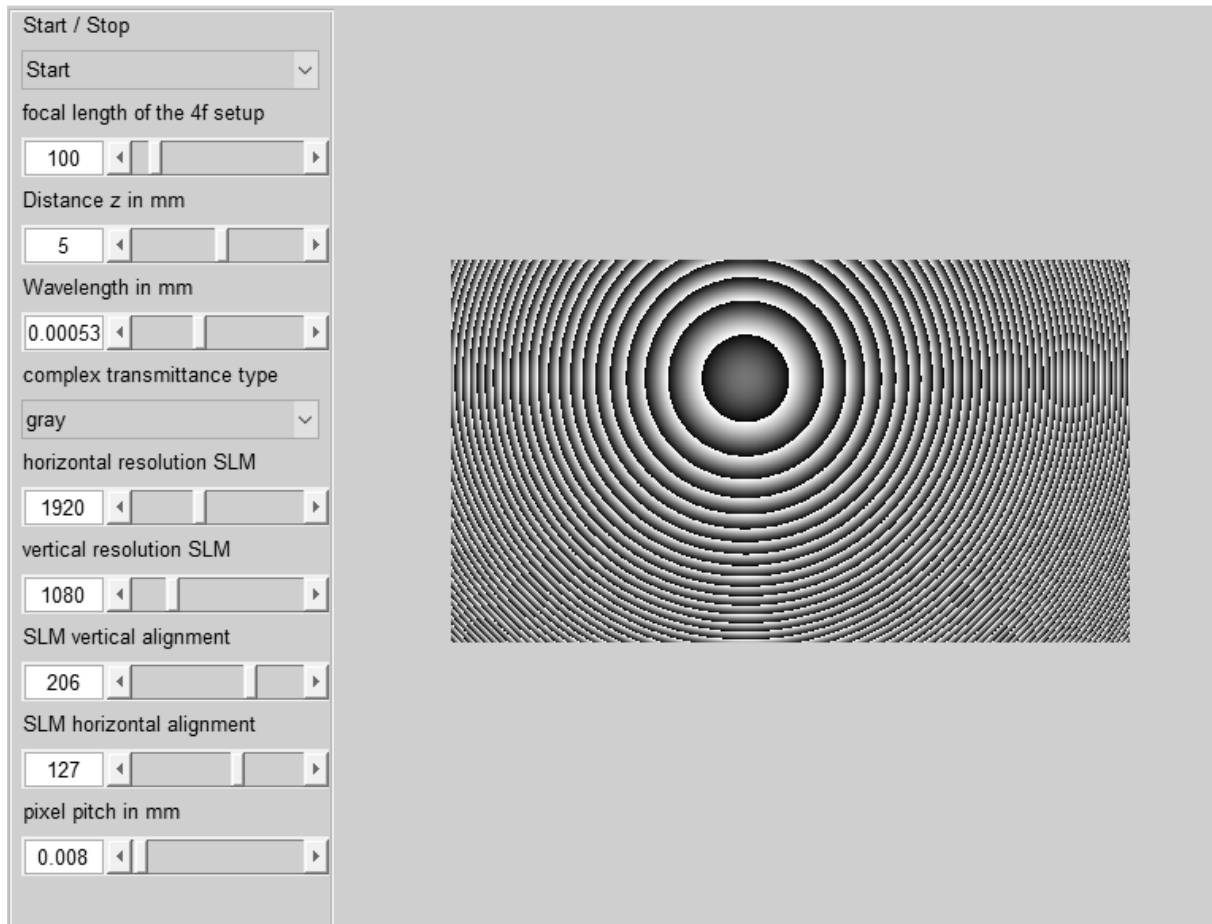
Appendix A.2: Program for controlling the spatial light modulator The program writes the transfer function of propagation according to the parameters set on the left onto the spacial light Modulator and displays a preview of the phase distribution as a greyscale image on the right. The tool was used in the calibration and misalignment compensation of the 4f setup and in obtaining all experimental results.

I operate the SLM with a program that I designed to write the transfer function of propagation onto the device. The program allows the workflow to be simplified significantly.

For reference, see Appendix Figure A.2. The parameters of the setup such a focal length f, wavelength λ, resolution and pixel pitch of the SLM can be set before the experiment takes place. The vertical and horizontal alignment values are necessary to compensate misalignment between the optical axes in the 4f setup. The propagation distance z can be set as well.

```matlab
% This script is an more developed version of Spice_Simulation_8_0 where it
% is attempted to simulate the spacial coherence aspect

%Speckle_Sim_2 Speckle simulation with spherical waves

clc; clear all; close all;

load('waveOrigin_2018-07-18');
%% GLOBAL: parameters

lambda = 0.00053;    %mm
ff = 100;            %mm

sourceDensity = 0.1;  %fraction of pixels that act as sources

surfaceVariance = 0.00003; %mm
zPlanes = -10;       %mm
radiusPlane_l = 1;   %mm
radiusPlane_r = 1;   %mm

apertureSize = 0.1;   %mm
Dp_slm = 0.008;      %mm
zSLM = 0;            %mm

%% SPECKLES: parameters

res = 1024;
dx = lambda*ff/(Dp_slm*res);      %pixel size (theses are chosen so that the sampling↙
of the SLM and the fft overlap)
du_4f = 1/(res*dx);    %pixel size in fourier domain in 1/mm for propagation of the↙
right plane



%% SPECKLES: Wavefield Calculation
NN = 100; %Number of Waves

%waveOriginX = ((rand(NN,1)*(res+1)-0.5)-res/2)*dx;
%waveOriginY = ((rand(NN,1)*(res+1)-0.5)-res/2)*dx;

%dz = randn(NN,1)*surfaceVariance;

[screenX, screenY] = meshgrid(dx*(-res/2+1:res/2), dx*(-res/2+1:res/2));

waveField = zeros(res);
intensityField = zeros(res);

u_z = zeros(res);

gamma = 0;
for ii = 1:NN
    sphericalWave = exp(1i*2*pi/lambda*sqrt((zPlanes+dz(ii)).^2+(screenX+waveOriginX↙
(ii)).^2 + (screenY+waveOriginY(ii)).^2));
    waveField = waveField + sphericalWave;
```